



1 **African dust transported to Barbados in the Wintertime Lacks Indicators of Chemical**
2 **Aging**

3

4 Haley M. Royer^{1,2}, Michael Sheridan^{1,3}, Hope Elliott^{1,4}, Nurun Nahar Lata⁵, Zezhen Cheng⁵,

5 Swarup China⁵, Zihua Zhu⁵, Andrew P. Ault⁶, Cassandra Gaston^{1*}

6 ¹Department of Atmospheric Sciences, Rosenstiel School of Marine, Atmospheric, and Earth
7 Science, University of Miami, Miami, FL

8 ²Department of Environmental Sciences and Engineering, University of North Carolina at
9 Chapel Hill, Chapel Hill, NC

10 ³Skidaway Institute of Oceanography, University of Georgia, Athens, GA

11 ⁴Department of Ocean Sciences, Rosenstiel School of Marine, Atmospheric, and Earth Sciences,
12 University of Miami, Miami, FL

13 ⁵Environmental Molecular Sciences Laboratory, Pacific Northwest National Laboratory,
14 Richland, WA

15 ⁶Department of Chemistry, University of Michigan, Ann Arbor, MI

16 *Corresponding Author:

17 Cassandra J. Gaston: Email: cgaston@miami.edu, Phone: (305)-421-4979

18

19

20

21

22

23

24

25



26 **1. Abstract**

27 The chemical processing (“aging”) of mineral dust is thought to increase dust light scattering
28 efficiency, cloud droplet activation, and nutrient solubility. However, the extent of African dust
29 aging during long-range transport to the western Atlantic is poorly understood. Here, we explore
30 African dust aging in wintertime samples collected from Barbados when dust is transported at
31 lower altitudes. Ion chromatography (IC) analysis of bulk nitrate, sulfate, and oxalate increase
32 when African dust reaches Barbados, indicating dust aging. However, aerosol mixing state
33 analysis from computer-controlled scanning electron microscopy with energy dispersive x-ray
34 spectroscopy (CCSEM/EDX) indicates that approximately 67% of dust particles are internally
35 mixed with sea salt, while only about 26% of dust particles contain no internally mixed
36 components. SEM/EDX elemental mapping and time-of-flight secondary ion mass spectrometry
37 (TOF-SIMS) reveals that within internally mixed dust and sea salt particles, only sea salt
38 components contain signs of aging.

39

40

41

42

43

44

45

46

47

48



49 2. Introduction

50 Upon emission, dust can directly scatter or absorb solar radiation (Balkanski et al., 2007;
51 Haywood et al., 2003; Myhre & Stordal, 2001; Sokolik et al., 2001; Tegen, 2003), act as cloud
52 condensation (Albrecht, 1989; Koehler et al., 2009; Zev Levin et al., 1996; Rosenfeld et al.,
53 2001) and ice nuclei (Archuleta et al., 2005; Cziczo et al., 2004; DeMott et al., 2003), and
54 provide micro- and macro- nutrients to nutrient-limited ecosystems (Elliott et al., 2024; Jickells
55 et al., 2005; Mahowald, 2011). However, mineral dust aerosol is still poorly represented in
56 climate models due, in part, to a lack of understanding of the physiochemical properties of dust
57 and their changes as a result of cloud processing (Gierlus et al., 2012; Wurzler et al., 2000),
58 multiphase reactions (Andreae et al., 1986; Sullivan et al., 2007; Sullivan & Prather, 2007) or
59 heterogeneous reactions with polluted air masses (Fitzgerald et al., 2015; Krueger et al., 2004;
60 Sullivan et al., 2009). The chemical change in the physiochemical properties of dust, herein
61 referred to as “aging”, can alter the water uptake properties of dust (Krueger et al., 2003; Laskin
62 et al., 2005) thus affecting its light scattering efficiency (Bauer et al., 2007; Kandler et al., 2011a;
63 Levin et al., 1996), cloud droplet activation properties (Gibson et al., 2007; Kelly et al., 2007;
64 Sullivan et al., 2009), and atmospheric lifetime (Abdelkader et al., 2015; Lance et al., 2013; Li et
65 al., 2014; Wu et al., 2013). Chemical aging is also essential to increase the bioavailability of
66 nutrients within dust via ligand-mediated and proton-mediated dissolution processes (Nenes et
67 al., 2011; Spokes & Jickells, 1995; Stockdale et al., 2016). Modeling the chemical aging process
68 is challenging and, as a result, models often treat dust as a chemically homogeneous and
69 hydrophobic particle type (Han et al., 2011; Pringle et al., 2010; Shi et al., 2008), which
70 oversimplifies the complexity of dust and its impacts in the atmosphere.



71 African dust is the largest source of dust, which is transported to the Caribbean, North
72 and South America and Europe (Barkley et al., 2019; Prospero & Mayol-Bracero, 2013). Most
73 research studying African dust transport focuses on the summer when dust mass concentrations
74 are at a maximum (Prospero & Mayol-Bracero, 2013; Zuidema et al., 2019) and the Saharan Air
75 Layer (SAL) that transports dust across the Atlantic is at its maximum altitude (Carlson &
76 Prospero, 1972). The height of African dust transport minimizes the mixing time of transported
77 dust with the underlying Marine Boundary Layer (MBL) until the dust settles out of the SAL
78 (Ryder et al., 2018). Studies exploring African dust aging during the summertime have produced
79 varying results. Early attempts to study dust aging in the western Atlantic from Li-Jones &
80 Prospero, 1998, found a strong correlation between mineral dust and non-sea salt sulfate (NSS-
81 SO_4^{2-}) from size-resolved filter measurements collected in Barbados during the boreal spring,
82 which they conclude is the result of dust aging by sulfur emissions from Europe. In more recent
83 studies, single-particle methods have been utilized to obtain more detail on the mixing state of
84 dust to unambiguously determine if markers of aging are located within dust or other aerosol
85 particles. Conclusions from Denjean et al., 2015, inferred from low hygroscopicity growth
86 measurements, that long range transported (LRT) African dust particles collected over Puerto
87 Rico in the boreal summer are not chemically processed and are minimally mixed with other
88 chemical components. In contrast, Fitzgerald et al., 2015 also analyzed LRT African dust in
89 Puerto Rico during the boreal summer, but found sulfate and oxalate on dust particles using real-
90 time single-particle mass spectrometry. Dust composition measured by Fitzgerald et al., 2015
91 may have also been affected by local cloud processing as sampling occurred within a cloud
92 forest. Boreal summer analysis of LRT dust in Barbados from Kandler et al., 2018 and
93 Weinzierl et al., 2017 revealed limited aging of dust particles with some internal mixing with



94 other chemical components from microscopy and spectroscopy analysis. Model analysis of
95 summertime African dust transport from Abdelkader et al., 2017 explored the evolution of dust
96 aging as dust is transported from Africa to the western Atlantic, finding that aged African dust is
97 quickly removed from the aerosol loading during transit across the Atlantic, leaving minimally-
98 aged dust within the aerosol loading that reaches the western Atlantic.

99 Unlike the summertime when dust is transported within the elevated SAL, dust is
100 transported at lower altitudes during the wintertime (Tsamalis et al., 2013) enhancing the mixing
101 time of dust within the MBL, which may increase the interaction between dust, anthropogenic
102 emissions, and marine biogenic emissions in the MBL (Gutleben et al., 2022; Savoie & Prospero,
103 1982). Additionally, the Sahelian burn season occurs during the boreal winter, often resulting in
104 long-range co-transport of dust and smoke emissions that were specifically observed during the
105 ATOMIC/EUREC⁴A campaigns (Quinn et al., 2021; Royer et al., 2023). Smoke emissions are
106 known to contain sulfur dioxide (SO₂) and nitrogen oxides (e.g., NO_x≡NO + NO₂) that
107 theoretically could age dust extensively (Hickman et al., 2021; Rickly et al., 2022), especially
108 during long-range transport in which dust has several days to interact with smoke emissions
109 before it arrives in the western Atlantic. During the ATOMIC/EUREC⁴A campaigns, sulfate was
110 observed on smoke particles, indicating a potential for dust aging during co-transport with smoke
111 (Royer et al., 2023). However, the likelihood of mixing between the emissions in the MBL, dust,
112 and African smoke emissions and their impact on dust aging during the wintertime is unclear.

113 The goal of this study is to determine the extent of aging on African dust particles
114 transported to the Caribbean during the boreal winter using methods that determine the mixing
115 state of individual particles. Collection of aerosol samples took place at the Barbados
116 Atmospheric Chemical Observatory (BACO) at Ragged Point, Barbados from January through



117 February of 2020 during the ATOMIC/EUREC⁴A campaign. During the sampling period, 3 dust
118 events consisting of co-transported dust and smoke originating from Africa arrived at Barbados,
119 offering ample opportunity to study the extent of aging. Lidar measurements also reveal that
120 dust-laden air masses remained at a low altitude (3.5 km) for the duration of their transit to
121 Ragged Point, contrasting high altitude summertime transport conditions (Gutleben et al., 2022).
122 This study provides a unique opportunity for exploring the extent of dust aging on African dust,
123 which should be at a maximum under the conditions described. Our findings provide much
124 needed insight into the extent of aging for African aerosols undergoing LRT to the western
125 Atlantic, which is essential for properly modeling the water uptake properties of dust particles in
126 the atmosphere as well as the solubility of nutrients in dust bearing minerals.

127 **3. Methods**

128 *3.1 Measurement Site and Sampling Period*

129 The sampling site, sampling period, and air mass origins that were studied have been
130 described previously in Royer et al., 2023. Briefly, aerosol samples consisting of long-range co-
131 transported African dust and smoke as well as marine aerosols were collected at the University
132 of Miami's Barbados Atmospheric Chemistry Observatory (BACO) at Ragged Point during the
133 EUREC⁴A and ATOMIC campaigns from 20 January through 20 February 2020 (Quinn et al.,
134 2021; Stevens et al., 2021). Air mass origins were determined using NOAA's HYSPLIT model
135 as well as daily dust mass concentrations. Ragged Point (13°6' N, 59°37'W), a prominence on
136 Barbados' eastern coast, is an ideal location for studying the extent of dust aging in LRT African
137 aerosols as it is exposed to the steady easterly trade winds which regularly carry outflows of
138 African aerosols such as dust and smoke to the island (Archibald et al., 2015; Carlson &



139 Prospero, 1972; Prospero, 1968) and minimize the influence of anthropogenic activity from local
140 islands to the west (Prospero et al., 2005; Savoie et al., 2002).

141 In this study, we utilize both bulk and single-particle methods to highlight the importance
142 of aerosol mixing state for understanding the extent of dust aging. Bulk methods have
143 traditionally been used to study long-range dust transport and the extent of dust aging in the
144 western Atlantic (Chen & Siefert, 2004; Li-Jones & Prospero, 1998; Savoie et al., 2002). Single
145 particle methods used herein show that elucidating the aerosol mixing state is essential for
146 determining the full extent of aging in LRT African dust particles.

147 *3.2 Dust Concentration and Soluble Ion Content*

148 To collect aerosol samples, the BACO is equipped with a high-volume sampler and an
149 isokinetic aerosol inlet on top of a 17 m-tall tower situated on a 30 m bluff along the coast at
150 Ragged Point. Aerosol filters were collected using a high-volume sampler pumping at a rate of
151 approximately 0.7 m³/min for bulk measurements and 1.0 m³/min for size-resolved
152 measurements. Size-resolved filters were collected on a cascade impactor (Tisch Environmental,
153 Inc., Series 230) with 6 stages and 1 backing filter. Size-resolved aerosol analysis are separated
154 into supermicron (stages 1-4; >1.3 μm) and submicron (stages 5 – backing filter; <1.3 μm). All
155 aerosol filter samples were collected on cellulose Whatman-41 (W-41) filters with a nominal 20
156 μm pore size. After filter collection, filters were washed with Milli-Q water three times to
157 remove soluble material. The washed filters were subsequently combusted in a furnace at 500 °C
158 for about 12 h (i.e., overnight) to remove the cellulose filter and determine daily dust mass
159 concentrations (Prospero et al., 2021; Zuidema et al., 2019). Procedural filter blanks were also
160 collected by placing a filter in the sampler cassette for 15 min without turning on the pump. The
161 resulting ash mass from a sample minus the mass of a filter blank is the gross ash weight, which



162 is then adjusted by a factor of 1.3 to convert the ash weight to a mineral dust concentration
163 (Prospero, 1999; Zuidema et al., 2019).

164 To determine daily bulk and size-resolved soluble ion content, the 20 mL of Milli-Q used
165 to wash the filters was filtered through a 25 mm membrane filter with 0.4 μm pore size
166 (Whatman Nuclepore Track Etch Membrane) to remove any particulates from the washing
167 process. Filtrate was then frozen in a -20°C freezer until analysis. To prepare samples, frozen
168 filtrate was thawed in a warm water bath and vortexed for 20 sec. The filtrate was then analyzed
169 using an ion chromatography (IC) instrument (Dionex Integrion HPIC System; Thermo
170 Scientific). Samples were analyzed in triplicate to ensure precision of results. To obtain soluble
171 ion content, 5 mL aliquots of filtrate were injected into the IC system and analyzed for cations
172 (IonPac CG12A/CS12A; Thermo Scientific) and anions (IonPac AS11-HC; Thermo Scientific).

173 Cations of interest analyzed by IC include lithium (Li^+), sodium (Na^+), ammonium (NH_4^+),
174 potassium (K^+), magnesium (Mg^+), and calcium (Ca^+) while anions of interest include fluoride
175 (F^-), formate (CH_2O^-), methanesulfonate (MSA), chloride (Cl^-), nitrite (NO_2^-), bromide (Br^-),
176 nitrate (NO_3^-), sulfate (SO_4^{2-}), oxalate, and phosphate (PO_4^{3-}). Since the filtrate analyzed includes
177 sea salt emissions, which may include sulfate from ocean emissions, non-sea salt sulfate (NSS-
178 SO_4^{2-}) was calculated using the equation

179
$$[\text{NSS} - \text{SO}_4^{2-}] = [\text{SO}_4^{2-}] - (0.2517 * [\text{Na}]) \quad (1)$$

180 to determine the fraction of sulfate derived from non-sea spray emissions including
181 anthropogenic and marine biogenic sources. For the purposes of this study, we focus primarily
182 on NSS- SO_4^{2-} and NO_3^- as they are chemical indicators of dust aging (Sullivan et al., 2007) as
183 well as oxalate as it indicates cloud processing and other processes (Ma et al., 2004). Samples
184 were also analyzed for methanesulfonate, an important tracer of ocean-derived biogenic sulfur



185 (Gaston et al., 2010) that can age dust particles (Desboeufs et al., 2024), however MSA

186 measurements were negligible.

187 *3.3 Aerosol Mixing State Analysis*

188 To determine the mixing state of individual particles, aerosol samples were collected at
189 ambient relative humidity (RH) through an isokinetic aerosol inlet with a three-stage
190 microanalysis particle sampler (MPS-3, California Measurements, Inc.), which samples particles
191 from diameters of 5.0-2.5 μm (stage 1), 2.5-0.7 μm (stage 2), and $<0.7 \mu\text{m}$ (stage 3). For each set
192 of samples (one set including one sample from each stage of the MPS), the MPS was run for 45
193 min at 2 L/min flow starting at approximately 09:30 LT (local time) or 13:30 coordinated
194 universal time (UTC). Meteorological data from a local station were used to manually check that
195 wind direction fell between 335 and 130 degrees and that wind speeds were greater than 1 m/s
196 during all sampling periods to ensure that only air from the open ocean to the east was sampled
197 rather than local, anthropogenically-influenced air.

198 *3.4 Single Particle Elemental Composition*

199 To determine aerosol elemental composition, particles were deposited onto carbon-coated
200 copper grids (Ted Pella, Inc., Prod. # 01910-F) on each of the 3 stages of the MPS that were later
201 analyzed at the Environmental Molecular Science Laboratory (EMSL) at Pacific Northwest
202 National Laboratory (PNNL) using computer-controlled scanning electron microscopy (Quanta
203 3D) coupled with energy-dispersive X-ray spectroscopy (EDAX, Inc.) (CCSEM/EDX).
204 Approximately 1800 particles from stage 1, 2500 particles from stage 2, and 3200 particles from
205 stage 3 were analyzed via CCSEM/EDX for each day of sampling. Only particles with diameters
206 $>0.1 \mu\text{m}$ were analyzed. Semiquantitative data products from CCSEM/EDX analysis were then
207 analyzed in MATLAB (version 9.6.0; The Mathworks, Inc.) using a k-means clustering



208 algorithm (Ault et al., 2012; Royer et al., 2023; Shen et al., 2016) to group similar particles into
209 clusters based on the elemental percentage, size, and shape of individual particles. These clusters
210 are then assigned to particle types based on their morphology, characteristic EDX spectra, and
211 the existing literature. Percent composition threshold values of 1% were used when processing
212 CCSEM/EDX data to ensure the presence of elements detected by the EDX. Single particle
213 analysis using CCSEM/EDX was limited to 16 elements found in common aerosols such as dust,
214 sea salt, and smoke particles: carbon (C), nitrogen (N), oxygen (O), sodium (Na), magnesium
215 (Mg), aluminum (Al), silicon (Si), phosphorus (P), sulfur (S), chlorine (Cl), potassium (K),
216 calcium (Ca), vanadium (V), manganese (Mn), iron (Fe), and nickel (Ni). To prevent the signal
217 from the Cu-grid from interfering with the particles, Cu was intentionally excluded from the list
218 of elements to detect. Though the grids are coated with C, C was intentionally included due to
219 the presence of organics within the aerosol loading. The inclusion of C may result in a
220 suppression of other elements of interest as the C signal may be artificially elevated by the C-
221 coating on the Cu-grids.

222 Particle identification was primarily based on semiquantitative elemental composition
223 determined by EDX. Dust particles were identified based on the presence of elements common
224 in aluminosilicate minerals, including Si, Al, Fe, K, Ca, and Mg detected from EDX analysis
225 (Hand et al., 2010; Krueger et al., 2004; Levin et al., 2005). Sea salt particles were characterized
226 by high Na and Cl content, indicating the presence of halite (NaCl). Internal mixtures of dust and
227 sea salt contained elements indicative of both dust (Si, Al, Fe, K, Ca, and Mg) and sea salt (Na
228 and Cl), usually with portions of the particle containing primarily dust with other portions
229 containing primarily sea salt. Internally mixed dust and smoke contained elements common in
230 mineral dust as well as high C, K, and S which are representative of carbon-based matter that has



231 undergone combustion and aging from sulfur compounds, leading to the formation of potassium-
232 containing salts (Andreae, 1983; Li et al., 2003).

233 Analysis of CCSEM/EDX data also included calculating the extent of aging across the
234 aerosol size distribution. To obtain this information, N and S % values for each particle in a
235 cluster of known particle type were extracted along with the corresponding diameter for each
236 particle. Data was then binned according to diameter size, while N and S % values were
237 averaged for each diameter size. Values that did not exceed 1% were rounded down to 0% as
238 only an exceedance of 1% guarantees the presence of an element.

239 The spatial distribution of elemental components on select particles was also determined
240 using elemental mapping (AZtecLive SmartMapping; Oxford Instruments). Approximately 10
241 elemental maps were collected for dust, sea salt, and internally mixed dust and sea salt. Spectra
242 were collected for select components within elemental maps to obtain more detailed chemistry
243 across an individual particle, which allows for analysis of sea salt and dust components as well
244 as the extent of aging in these components within internally mixed dust and sea salt particles.

245 *3.5 Aerosol Surface Chemical Composition*

246 The spatial distribution of major ions across the surface of individual particles was also
247 determined. Aerosol particles were collected onto silicon wafers (Ted Pella, Inc., Prod. # 16008)
248 within the MPS, which were then analyzed with time-of-flight secondary ion mass spectrometry
249 (TOF-SIMS; IONTOF GmbH, Munster, Germany) at PNNL (Li et al., 2023). In addition to
250 providing more detailed chemical information on dust aging, TOF-SIMS supplements the time-
251 intensive method of elemental mapping with SEM/EDX by analyzing multiple particles to
252 explore particle aging, thus supporting the representativeness of elemental mapping results to the
253 total aerosol loading (Hopkins et al., 2008). Further, while EDX is limited to elemental data



254 indicative of aging (e.g., the presence of N and/or S), TOF-SIMS can detect compounds such as
255 nitrate (NO_3^-) and sulfate (HSO_4^-) ions that more concretely provide evidence of chemical aging.

256 To perform TOF-SIMS analysis, a 25 keV Bi_3^+ beam was focused to around a 0.4 μm
257 diameter area on the silicon substrate and scanned over a $100 \mu\text{m} \times 100 \mu\text{m}^2$ area to produce an
258 image of 256×256 pixels. The current of the beam was 0.36 pA with 10 kHz pulse frequency,
259 and data collection time was 600 s per set of images. The total ion dose for each sample was
260 under the static limit so that only surface information ($< 2 \text{ nm}$) was collected for the analyzed
261 particles. Delayed extraction mode was also used during image collection to ensure that both
262 positive and negative ion images could be collected at the exact same location. Ions of interest
263 indicated the presence of sea salt (Na_2Cl^+ and NaCl_2^-), dust (Al^+ and Ca^+), and chemical aging
264 (HSO_4^- and NO_3^-). Surface contamination from the lab space the samples were handled in (e.g.,
265 butanediol (m/z -89) likely from butanol used in particle counters in the lab space) was observed
266 in the samples, and to remove contamination, a 20 keV argon (Ar) cluster ($\text{Ar}_{1500 \pm 300}^+$) sputtering
267 ion beam was used with a beam current of about 2.0 nA before chemical analysis with the 25
268 keV Bi_3^+ beam occurred. Samples underwent Ar sputtering for 50s to remove the top 100 nm of
269 sample.

270 4. Results

271 4.1 Bulk Aerosol Analysis

272 Figure 1 presents daily dust mass concentrations and bulk soluble ion content along with
273 correlation plots for each ion of interest. Results show a strong correlation between daily dust
274 mass concentrations and nitrate (NO_3^- , $R^2 = 0.75$) and non-sea salt sulfate (NSS-SO_4^{2-} , $R^2 =$
275 0.83), as well as a weak correlation with oxalate ($R^2 = 0.11$) throughout the entire campaign. The
276 presence of nitrate, non-sea salt sulfate, and oxalate from bulk aerosol analysis suggests that dust



277 is being aged during transport. Similar figures for supermicron and submicron analysis can be
278 found in Figures S1 and S2, respectively, in the Supporting Information (SI). Notably, dust mass
279 concentrations were evenly split between the supermicron and submicron size modes. Both
280 supermicron (*SUP*) and submicron (*SUB*) analysis shows similar findings to bulk filter analysis
281 in which a strong correlation exists between dust mass concentrations and nitrate ($R^2_{\text{SUP NO}_3} =$
282 0.50 ; $R^2_{\text{SUB NO}_3} = 0.59$), non-sea salt sulfate ($R^2_{\text{SUP NSS-SO}_4} = 0.80$; $R^2_{\text{SUB NSS-SO}_4} = 0.49$), and
283 oxalate ($R^2_{\text{SUP oxalate}} = 0.63$; $R^2_{\text{SUB oxalate}} = 0.27$). Differences between supermicron and submicron
284 analysis indicate that nitrate is more concentrated in the supermicron aerosol loading ($\text{Avg}_{\text{SUP NO}_3}$
285 $= 0.64 \mu\text{g}/\text{m}^3$; $\text{Avg}_{\text{SUB NO}_3} = 0.44 \mu\text{g}/\text{m}^3$). However, nitrate has an appreciable submicron mode
286 likely due to transported African smoke. Results also show that NSS-SO_4^{2-} ($\text{Avg}_{\text{SUP NSS-SO}_4} =$
287 $0.04 \mu\text{g}/\text{m}^3$; $\text{Avg}_{\text{SUB NSS-SO}_4} = 0.46 \mu\text{g}/\text{m}^3$) and oxalate ($\text{Avg}_{\text{SUP oxalate}} = 0.01 \mu\text{g}/\text{m}^3$; $\text{Avg}_{\text{SUB oxalate}} =$
288 $0.04 \mu\text{g}/\text{m}^3$) are more concentrated in the submicron aerosol loading (Quinn et al., 2021; Royer et
289 al., 2023; Savoie et al., 1982). These findings suggest that dust is possibly being aged, with
290 supermicron dust being primarily aged by nitrate and submicron dust being primarily aged by
291 sulfate and oxalate or via cloud processing (Bondy et al., 2017). However, the limitations of this
292 traditional analysis include an oversimplification of aerosol mixing state by assuming nitrate,
293 non-sea salt sulfate, and oxalate are associated only with dust.

294 *4.2 Size-Resolved Aerosol Mixing State*

295 Using size-resolved chemical data of individual particles from CCSEM/EDX analysis,
296 we assessed the extent of aging across the aerosol size distribution. The role of particle size is
297 important as smaller dust particles have higher surface area-to-volume ratios that have been
298 suggested to increase the propensity for dust aging (Baker & Jickells, 2006). Results from
299 CCSEM/EDX analysis revealed the presence of both marine particles such as sea spray, aged sea



300 spray, organics, and sulfates, as well as continental particle types including dust, internally
301 mixed dust and sea salt, internally mixed dust and smoke, and smoke that are described in detail
302 in Royer et al., 2023. Here, we focus on 4 particle types relevant to the understanding of dust
303 aging during the sampling period: dust, sea spray (combined sea spray and aged sea spray),
304 internally mixed dust and sea salt, and internally mixed dust and smoke.

305 Figure 2 presents detailed size-resolved chemical data for the four particle types of
306 interest during periods of dust transport to Barbados, providing insight into the extent of particle
307 aging across the aerosol size distribution. In Figure 2a, particle types are plotted as number
308 fractions of the aerosol loading as a function of aerosol diameter. Number fractions of dust
309 particles determined from CCSEM analysis contrast dust mass concentrations determined from
310 bulk aerosol analysis. Dust mass concentrations for the submicron and supermicron aerosol
311 loading are similar at $14.38\mu\text{g}/\text{m}^3$ and $12.28\mu\text{g}/\text{m}^3$, respectively. However, CCSEM analysis
312 reveals a large difference in the number fractions of submicron and supermicron dust particles,
313 where dust only makes up 21% and 4% of the submicron and supermicron aerosol loading by
314 particle number, respectively. This discrepancy is not only due to the difference in individual
315 particle mass between sub- and supermicron particles, but also due to the oversimplification of
316 dust particles in bulk analysis. Figure 2a reveals that internal mixtures of dust with other
317 components such as sea salt and smoke are, in fact, more abundant in the aerosol size distribution
318 compared to dust alone, specifically in the supermicron aerosol loading. Internal mixtures of dust
319 and sea salt comprise 11% of the submicron and 45% of the supermicron aerosol loading, while
320 internal mixtures of dust and smoke comprise 14% of the submicron and 8% of the supermicron
321 aerosol loading. These data reveal a complexity in the aerosol loading overlooked by bulk



322 aerosol analysis, and call into question the assumption that the presence of nitrate, non-sea salt
323 sulfate, and oxalate in bulk samples indicates aging of individual dust particles.

324 Figures 2b, c, d, and e present the average detectable N content (left axis) and number
325 fraction of N-containing particles (right axis) as a function of size for sea salt, internally mixed
326 dust and sea salt, internally mixed dust and smoke, and dust particles, respectively. Values for
327 average N content and particle fractions with detectable N for each particle type are reported in
328 the Supporting Information (SI) tables S1 and S2, respectively. Notably, average N content
329 within individual particles is similar for all 4 particle types, ranging from $2.0 \pm 0.5\%$ to $2.6 \pm 0.4\%$
330 N with an average N content of $2.2 \pm 0.6\%$. However, between the 4 particle types, there are large
331 variations in the number of particles containing detectable N. Detectable N is found in $36 \pm 25\%$
332 of submicron and $76 \pm 12\%$ of supermicron dust particles. This corroborates findings from bulk
333 aerosol analysis which shows that nitrate is more concentrated in the supermicron aerosol
334 loading compared to the submicron aerosol loading. However, figure 2a reveals that dust only
335 comprises 13% of the aerosol loading by number, with a much larger contribution in the
336 submicron aerosol loading. Considering that individual particles containing detectable N on
337 average have a N content of $2.2 \pm 0.6\%$, dust alone cannot explain trends in bulk nitrate. Figure
338 2c, d, and e all indicate the presence of N in particles aside from dust. Most notably, internally
339 mixed dust and sea salt, which makes up 45% of the supermicron aerosol loading, has detectable
340 N in $75 \pm 14\%$ of supermicron particles, potentially explaining the high supermicron nitrate
341 content from bulk aerosol analysis.

342 Figures 2f, g, h, and i present the average detectable S content and number fraction of S-
343 containing particles for the 4 particle types of interest. Values for average S content and particle
344 fractions with detectable S for each particle type are reported in SI tables S3 and S4,



345 respectively. Similarly to Figures 2b, c, d, and e, the S plots indicate that S content in individual
346 particles does not vary much across the aerosol size distribution for each particle type, with
347 average S content for the total aerosol loading ranging from $1.7 \pm 0.5\%$ to $2.7 \pm 0.5\%$ and
348 averaging $2.4 \pm 1.2\%$. However, particle fractions with detectable S do vary across the aerosol
349 size distribution and between particle types. Only $8 \pm 7\%$ of submicron and $14 \pm 15\%$ of
350 supermicron dust particles contained detectable S, indicating a large discrepancy between dust
351 particles containing S and the S mass concentrations observed. For almost all particle types
352 across the aerosol size distribution, with the exception of supermicron internal mixtures of dust
353 and smoke, S content exceeds that of dust. Internal mixtures of dust and sea salt far exceed the S
354 content in dust with $28 \pm 9\%$ of submicron particles and $35 \pm 19\%$ of supermicron particles
355 containing S. This is especially relevant as internal mixtures of dust and sea salt comprise a
356 much larger portion of the supermicron aerosol loading at 45%, compared to dust at 4%. Sea salt
357 particles, which also make up a much larger portion of the particle loading than dust at 55% of
358 the submicron and 44% of the supermicron aerosol loading, also contained larger number
359 fractions of particles with detectable S where $36 \pm 22\%$ of submicron and $87 \pm 58\%$ of supermicron
360 sea salt particles had observable S. However, an increase in S in sea salt particles across the size
361 distribution is likely the result of calcium-sulfate minerals that often form on larger sea salt
362 particles (Ault et al., 2013; Bondy et al., 2018; Choël et al., 2007). Observed S in sea salt and
363 internal mixtures of dust and sea salt may explain the observed non-sea salt sulfate mass
364 concentrations in the supermicron size range. However, number fractions of particles containing
365 detectable S were greater in the supermicron size range compared to the submicron size range for
366 all four particle types except internally mixed dust and smoke. Internally mixed dust and smoke
367 only comprises 14% of the submicron aerosol loading and has an average S content of $2.7 \pm 1.0\%$



368 for submicron particles. Instead, high mass concentrations of sulfate observed in submicron IC
369 analysis are likely caused by ammonium sulfate particles observed during the sampling period.
370 Previous studies show sulfate particles are primarily submicron in size and comprise a large
371 fraction of the submicron aerosol loading during both clean marine conditions and African dust
372 transport, which may contribute high non-sea salt sulfate mass detectable in bulk aerosol analysis
373 but not in S content for the four particle types of interest (Royer et al., 2023).

374 Ternary plots presented in Figure 3 provide insight into the chemical mixing state of
375 detected particles during the EUREC⁴A/ATOMIC campaign. Single particles are represented by
376 individual dots in each ternary plot. The color of each dot indicates the diameter of the particle it
377 represents. The position of each dot within the ternary plot indicates the relative abundance of S
378 (left vertex), Cl (top vertex), and N (right vertex) within each particle. Sea salt particles
379 displayed in Figure 3a are clustered primarily at the top vertex indicating high Cl content, low S
380 content, and low N content characteristic of freshly emitted sea salt. Particle clustering at the left
381 and right vertices demonstrates aging of sea salt particles as low Cl content and high S and/or N
382 content suggests chloride has been depleted and replaced with nitrate and sulfate during
383 heterogeneous reactions (Ault et al., 2013, 2014; Behnke et al., 1997; Gaston et al., 2011, 2013;
384 Sobanska et al., 2003). Differences in color at each vertex within Figure 3a also indicates that
385 aged sea salt particles are smaller than fresh sea salt particles on average (Laskin et al., 2012).

386 Dust and internally mixed dust and smoke particles are primarily in the submicron size
387 range, as indicated in Figure 2, and cluster at the right vertex indicating the presence of more
388 nitrate compared to sulfate and chloride in these particles, but these particles are sparse in
389 number concentration. Internally mixed dust and sea salt particles cluster primarily along the
390 right axis of the ternary plot, exhibiting various levels of Cl likely from sea salt, low S, and



391 varying N content. Notably, larger particles identified as internally mixed dust and sea salt had
392 elevated chloride compared to S and N while smaller particles had less chloride and elevated S
393 and N. Figure 3 demonstrates that, of the particle types containing dust components, internal
394 mixtures of dust and sea salt are the most abundant in the aerosol loading and had the highest
395 number of aged particles containing detectable N and S. As such, we focus our analysis of
396 chemical aging on internally mixed dust and sea salt.

397 *4.3 Elemental Mapping*

398 While analysis by CCSEM/EDX is valuable for determining size-resolved aerosol mixing
399 state, this method does not map the distribution of elements within each particle, which leads to
400 uncertainty regarding the location of the aging components within the particles, particularly for
401 internally mixed particle types. The elemental mapping image depicted in Figure 4a shows the
402 distribution of elements across an entire particle. The presence of distinct areas of dust
403 components such as Si, Al, Ca, Fe, and Mg that are separate from sea salt components such as
404 Na and Cl within a single particle indicates that the particle is a typical internally mixed dust and
405 sea salt particle. Within the image, the distribution of nitrogen and sulfur are depicted as well,
406 and visually appear present only over the sea salt components. Spectra from EDX analysis were
407 extracted from these distinct regions on the particle which reveal that nitrogen and sulfur are
408 indeed either negligible or completely absent on the dust components (S = 0.1%; N = 0%), while
409 they are present in appreciable quantities on the sea salt components (S = 2.9%; N = 2.9%). Also
410 worth noting is the absence of Cl in the sea salt component, which is indicative of sea salt aging
411 also observed in CCSEM/EDX analysis. This particle is representative of internally mixed dust
412 and sea salt particles detected during the sampling period that similarly show only aging on the
413 sea salt components. Additional examples of internally mixed dust and sea salt particle elemental



414 maps and EDX spectra are provided in Figure S3 of the SI. In addition, elemental maps and
415 corresponding EDX spectra for dust, sea salt, smoke, and internally mixed dust and smoke are
416 provided in Figure S4. Similar to the internally mixed dust and sea spray particles, externally
417 mixed dust and the dust component that is internally mixed with smoke show a lack of aging
418 while the smoke components in mixed dust and smoke particles show extensive accumulation of
419 sulfate. These results suggest that even in internal mixtures of dust, only the sea salt (or smoke)
420 components are undergoing ageing while dust is unprocessed

421 *4.4 TOF-SIMS Imaging*

422 Results from TOF-SIMS analysis corroborate findings from SEM/EDX elemental
423 mapping, indicating that aging of internally mixed dust and sea salt particles occurs primarily on
424 the sea salt components. Figure 5 depicts results from TOF-SIMS imaging in which the color
425 intensity in each image represents the intensity of an ion. The cation images in the top panel
426 indicate the presence of sea salt (Na_2Cl^+) and dust (Al^+ and Ca^+), while the last cation image on
427 the righthand side shows all ions plotted together. The cation image indicates that while the
428 majority of the particles in the image presented are sea salt particles due to the abundance of
429 Na_2Cl^+ , the co-location of sea salt components with dust components Al^+ and Ca^+ suggest there
430 is internal mixing of dust and sea salt as well. The anion images in the bottom panel similarly
431 plot individual ions, with the anions indicating the presence of sea salt (NaCl_2^-) and chemical
432 markers of aging from sulfate and nitrate (HSO_4^- and NO_3^- , respectively) as well as a final image
433 containing all anions plotted together. Once again, the presence of the anion NaCl_2^- suggests that
434 sea salt is abundant and further corroborates the cation images. The presence of HSO_4^- and NO_3^-
435 provide insight into the extent of aging on the particles presented in the images which show a
436 strong presence of aging from sulfate through the presence of HSO_4^- but a lack of aging from



437 nitrate through the absence of NO_3^- . Most notably, in the image overlaying all anions together,
438 the NaCl_2^- and HSO_4^- are indistinguishable from one another, indicating aging on the sea salt
439 components. Comparing the cation image to the anion image, it is clear that the areas in which
440 dust components are present are not undergoing aging, rather, primarily the sea salt components
441 are being aged. This supports findings from elemental mapping from SEM/EDX analysis which
442 similarly suggest minimal aging of dust components but aging of sea spray components in these
443 internally mixed particles.

444 **Discussion & Conclusion**

445 Traditional methods for studying dust aging often measure dust concentrations (or their
446 proxies) and soluble materials extracted from aerosol filters that oversimplify the aerosol
447 loading. Previous studies have historically used correlations between nss-sulfate, oxalate, and
448 nitrate and dust mass concentrations to prove the presence of dust aging, but have been unable to
449 determine the mixing state of dust and, thus, whether the dust is actually undergoing aging with
450 traditional methods (Chen & Siefert, 2004; Li-Jones & Prospero, 1998). The results from this
451 work indicate that while internal mixtures of dust with other particles are common in the lower
452 boundary layer, both internally and externally mixed African dust detected in the western
453 Atlantic are minimally aged during the wintertime. The boreal winter provides the most ideal
454 conditions for African dust aging to occur due to the lower transport altitude creating more time
455 for MBL emissions to interact with LRT dust. Further, wintertime dust is often co-transported
456 with Sahelian biomass burning emissions contributing high concentrations of NO_x and SO_2 that
457 are co-transported with dust, allowing for interaction of dust with aging components over several
458 days during its transit to the western Atlantic (Hickman et al., 2021). The lack of aging on
459 internal mixtures of dust and smoke indicate rapid conversion of NO_x and SO_2 to nitrate and



460 sulfate on smoke, which is corroborated by the presence of potassium sulfate salts observed on
461 smoke particles from EUREC⁴A/ATOMIC and a lack of these compounds on dust (Royer et al.,
462 2023). The lack of dust aging indicators observed during the winter may indicate a lack of aging
463 throughout the year for LRT African dust. This is apparent from size-resolved CCSEM/EDX
464 data which indicate a lack of aging on dust particles by sulfate and nitrate, and from elemental
465 mapping and TOF-SIMS imaging which show that chemical aging is favored on the sea spray
466 and smoke components of internally mixed dust particles.

467 It is likely that dust is being aged in the eastern Atlantic, but is removed during LRT to
468 the western Atlantic based on previous studies (Abdelkader et al., 2017). Further, it is likely that
469 any aging that occurs on dust in the eastern Atlantic is removed during LRT to the western
470 Atlantic. The lower altitude for dust transport during the wintertime would also provide ample
471 opportunity for dust aging in the eastern Atlantic which could lead to the rapid aging of dust
472 particles before LRT (Chiapello et al., 1995; Kandler et al., 2011; Ullerstam et al., 2002). The
473 addition of high levels of pollutants from the Sahelian fires could also exacerbate aging in the
474 eastern Atlantic (Andreae et al., 2000). Aged dust particles are much more efficiently removed
475 by both wet and dry deposition as well as cloud droplet activation as a result of increased water
476 uptake properties enhancing their size and reactivity (Abdelkader et al., 2017; Gaston, 2020;
477 Metzger et al., 2006). It is possible that the rapid aging of dust particles in the eastern Atlantic
478 upon dust emission increases the water uptake properties of the dust, leading to rapid removal of
479 dust particles before LRT can carry dust particles to the western Atlantic. This potentially
480 explains the lack of aging on dust particles in the western Atlantic, as any aged dust is likely
481 removed before arriving over Barbados.



482 Based on the high abundance of internally mixed dust and sea salt particles in the aerosol
483 loading, it is likely that unaged dust transported across the Atlantic becomes associated with
484 aged sea spray as dust is being detrained from from the SAL into the MBL as observed in
485 previous studies (Abdelkader et al., 2017). This would result in altitudinal gradients in dust
486 mixing state important for dust radiative impacts. Though dust components in the lower
487 boundary layer are rarely aged, internal mixtures of dust with other components such as sea salt
488 and smoke are common. The high degree of aging on these internally mixed components suggest
489 internal dust mixtures are more hygroscopic and thus are potentially efficient as cloud
490 condensation nuclei.

491 The lack of aging on dust components has implications for nutrient availability in mineral
492 dust aerosols transported to the tropical Atlantic as well. Ecosystems in the tropical Atlantic such
493 as the open Atlantic Ocean and the Amazon rainforest rely on external inputs of nutrients such as
494 iron and phosphorus (Fe and P). Chemical aging is particularly important to provide bioavailable
495 sources of nutrients to marine ecosystems, as deposition of particles out of the euphotic zone
496 competes with nutrient release into seawater (Gaston, 2020). The lack of aging on mineral dust
497 observed in this study suggests African dust may not be as important of a source of bioavailable
498 nutrients for the North Atlantic as previously assumed.

499 In this work, we utilized methods that target aerosol mixing state to determine the extent
500 of aging in LRT African dust particles to the western Atlantic during the wintertime. The
501 disparity between bulk methods, which suggest dust aging is extensive, and methods that
502 characterize the aerosol mixing state, which reveal a distinct lack of aging for dust components,
503 reveals the importance of utilizing single-particle methods to understand dust aging (Fitzgerald et
504 al., 2015; Kandler et al., 2011). We also provide much-needed insight into the question of dust



505 aging in the western Atlantic, revealing a lack of aging for dust particles in the wintertime that
506 should be considered in global and regional models.

507 **Data Availability**

508 The data will be publicly available in the University of Miami data repository.

509 **Author Contribution:**

510

511 Conceptualization of this was performed by HMR, APA, and CJG. Collection of samples was
512 conducted by HMR, while analysis was done by HMR, MS, HE, NNL, ZC, and ZZ. Development
513 of methods used in this work was done by HMR, ZC, SC, APA, and CJG. Instrumentation used to
514 conduct this work was provided by CJG, APA, SC, and ZZ. Validation of data products was
515 performed by HMR, ZC, APA, and CJG. Computer code used for data analysis was provided by
516 APA. Data visualization was performed by HMR, APA, and CJG. Supervision and project
517 administration duties were conducted by CJG. CJG is solely responsible for funding acquisition.
518 HMR wrote the original draft for publication, and all co-authors reviewed and edited this work.

519

520 **Competing Interests:** The authors declare that they have no conflict of interest.

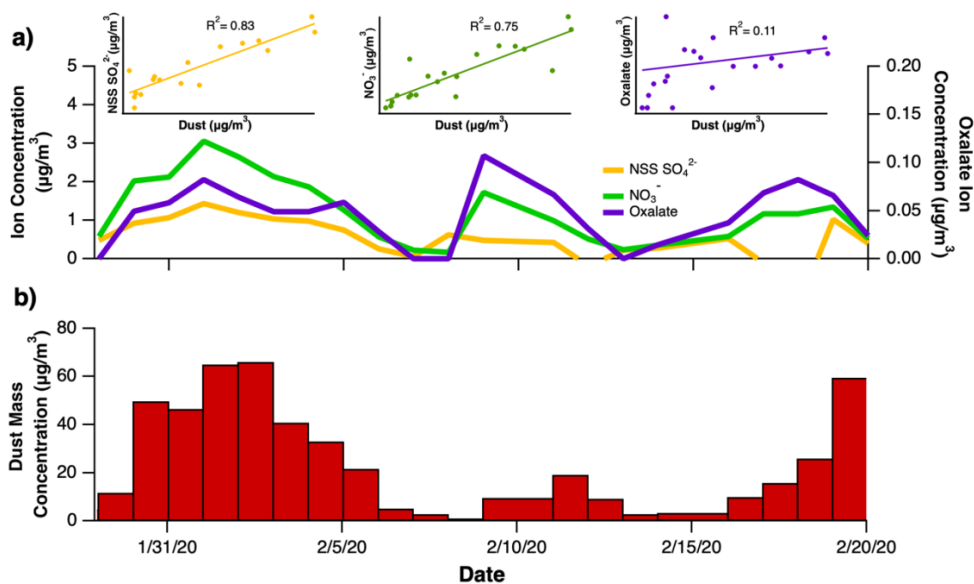
521

522 **Acknowledgements**

523 C.J.G. acknowledges an NSF CAREER award (1944958). A portion of this research was
524 performed on project awards (10.46936/lser.proj.2019.50816/60000110 and
525 10.46936/lser.proj.2021.51900/60000361) from the Environmental Molecular Sciences
526 Laboratory, a DOE Office of Science User Facility sponsored by the Biological and
527 Environmental Research program under Contract No. DE-AC05-76RL01830.

528

529



530

531 Figure 1 – Daily bulk soluble ion content for nitrate (left axis; green line), non-sea salt sulfate

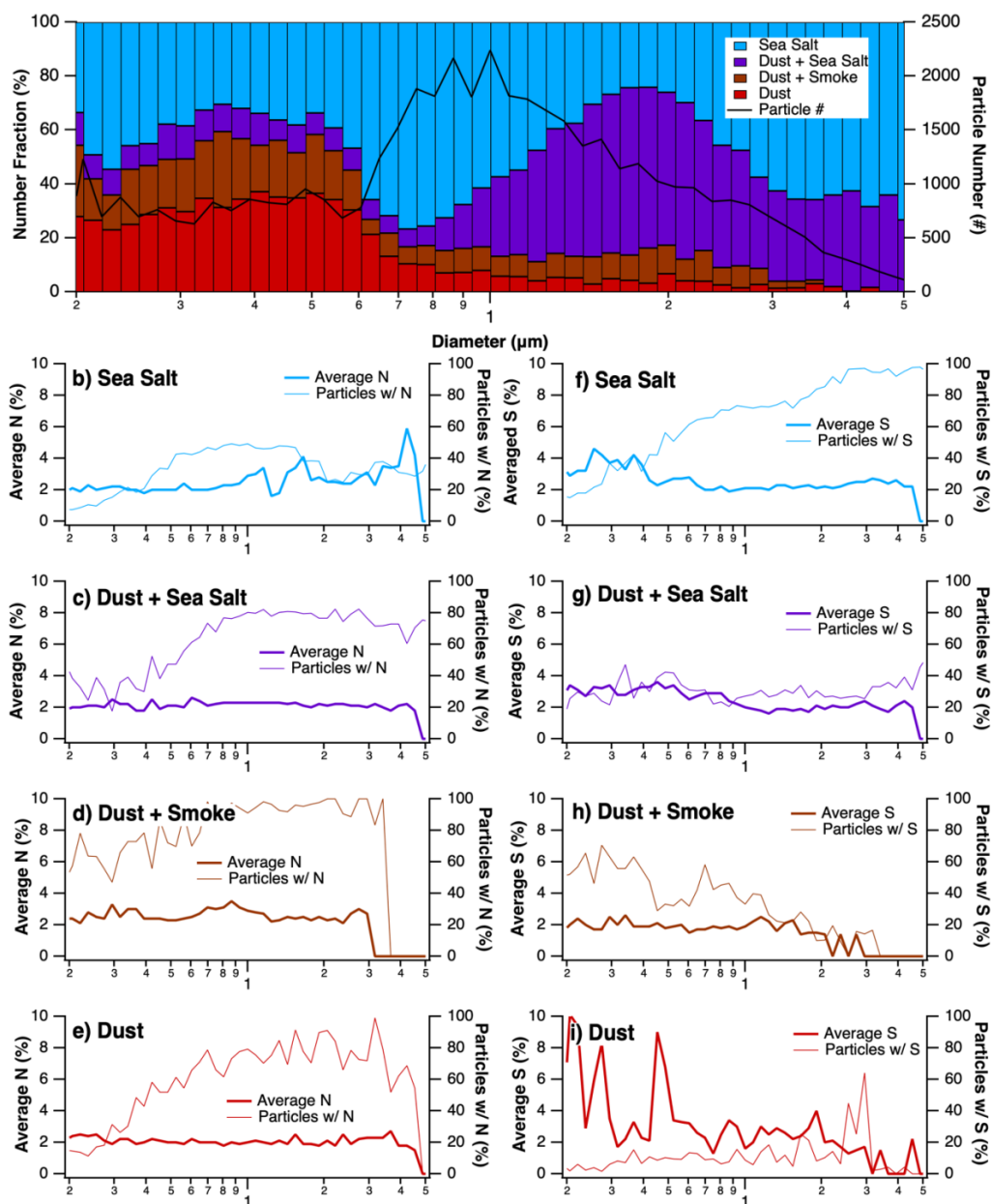
532 (left axis; yellow line), and oxalate (right axis; purple line) with correlation plots for each ion as

533 a function of dust mass concentrations a) and daily bulk dust mass concentrations b) determined

534 for the entire sampling period. Correlation plots include all data, including data from samples

535 with undetectable ions, but trendlines only consider data with detectable dust and ions.

536



537

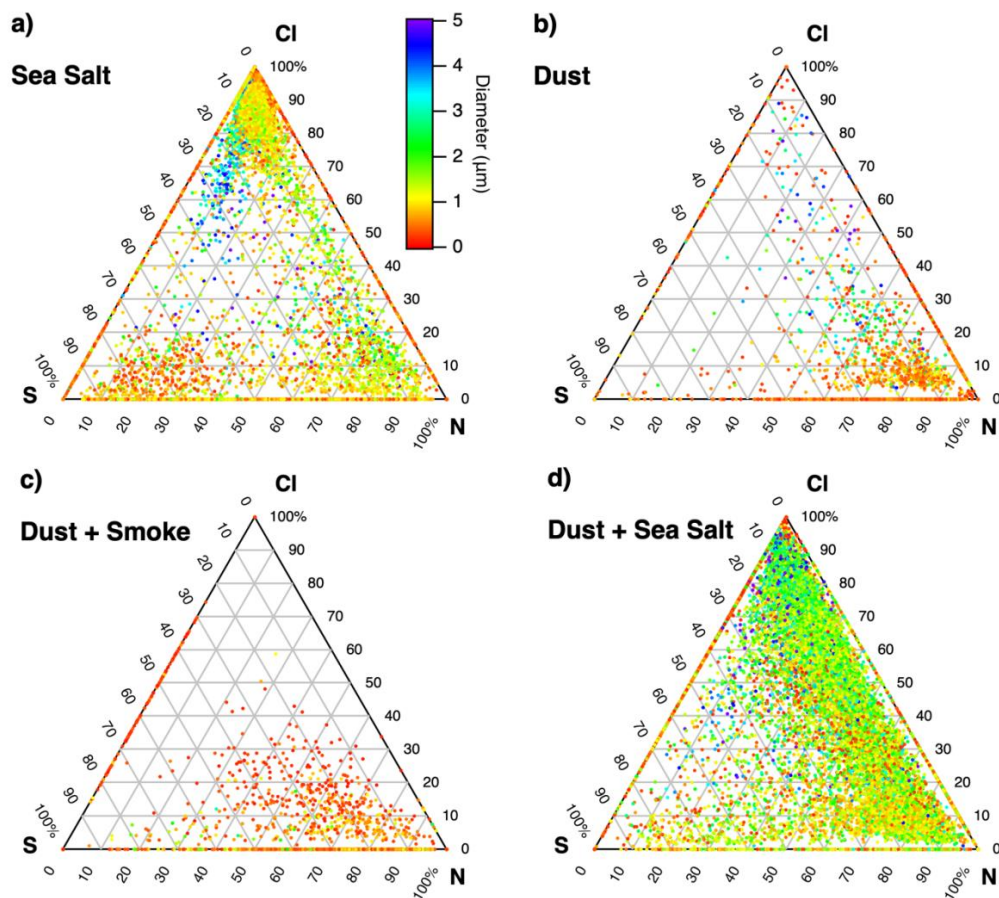
538 Figure 2 – Size-resolved chemistry plots summarized by a) a total size-resolved chemistry plot in

539 which the particle number loading is normalized to the sum of sea salt particles (blue), internally

540 mixed dust and sea salt particles (purple), internally mixed dust and smoke particles (brown), and

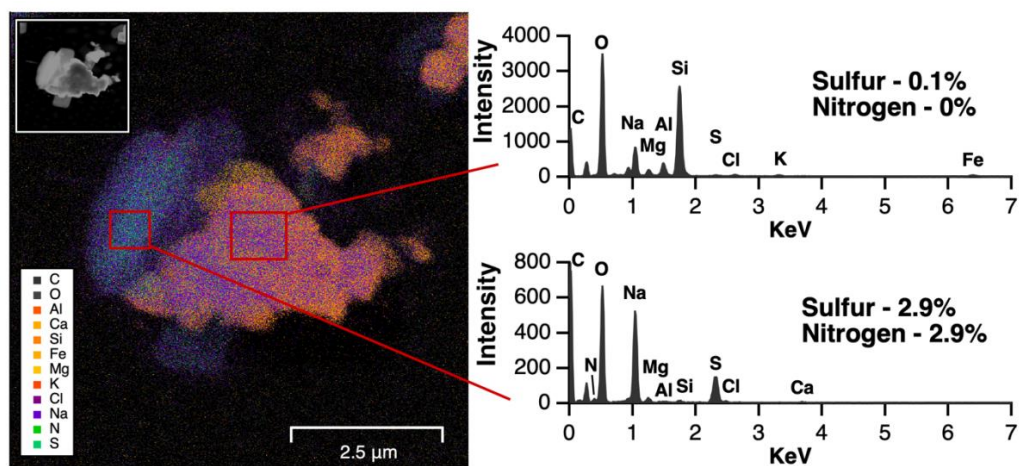


541 dust particles (red) for each size bin and presented as a fraction of the particle number loading in
542 each size bin (left axis) along with the total sum of the number of particles of interest for each
543 size bin (right axis: black line). Plots depicting the average N or S content in individual particles
544 (left axis; thick line) as well as the number fraction of particles in each size bin containing N or S
545 (right axis; thin line) are provided for b) N in sea salt particles, c) N in internally mixed dust and
546 sea salt particles, d) N in internally mixed dust and smoke particles, e) N in dust particles, f) S in
547 sea salt particles, g) S in internally mixed dust and sea salt particles, h) S in internally mixed dust
548 and smoke particles, and i) S in dust particles.



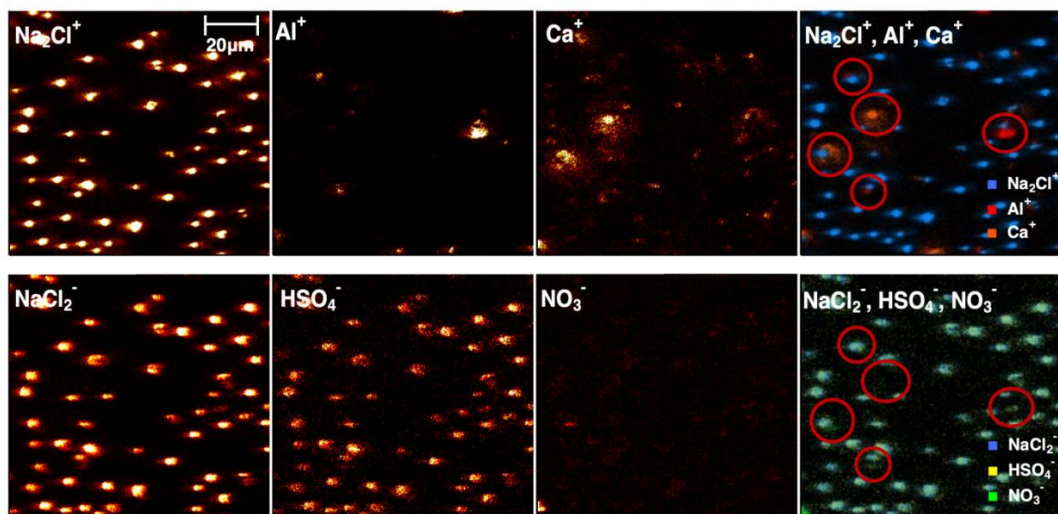
549

550 Figure 3 – Ternary plots presenting the normalized percentage of S (left axis), Cl, (right axis),
551 and N (bottom axis) present in dust (6426 particles), internally mixed dust + smoke (N=1588 pt),
552 internally mixed dust + sea salt (18,210 particles), and sea salt (22,354 particles). Color scaling
553 denotes particle diameter.



554

555 Figure 4 – Elemental mapping image from SEM/EDX analysis for an internally mixed dust and
556 sea salt particle collected at Ragged Point on 2/9/2020 on stage 2 of the MPS. Top left plot
557 depicts the SEM image. The legend explains the color associated with each element plotted in
558 the elemental map with warm colors denoting dust components, cool colors denoting sea spray
559 components and green colors denoting aging markers (a). Red squares on the elemental map
560 indicate where EDX spectra were extracted for the dust component (b) and the sea salt
561 component (c) of the particle. Sulfur and nitrogen values represent calculated EDX intensity
562 present on dust and sea spray components of the particle.



563

564 Figure 5 – Image plots from TOF-SIMS analysis of a sample collected on 2/18/2020 from stage

565 1 of the MPS. Red circles mark the location of dust components of the particles.

566

567

568

569

570

571

572

573

574

575

576

577

578

579

580

581

582

583

584

585

586

587



588 **References**

589

590 Abdelkader, M., Metzger, S., Mamouri, R. E., Astitha, M., Barrie, L., Levin, Z., & Lelieveld, J.

591 (2015). Dust–air pollution dynamics over the eastern Mediterranean. *Atmospheric*
592 *Chemistry and Physics*, 15(16), 9173–9189. <https://doi.org/10.5194/acp-15-9173-2015>

593 Abdelkader, M., Metzger, S., Steil, B., Klingmüller, K., Tost, H., Pozzer, A., Stenchikov, G.,
594 Barrie, L., & Lelieveld, J. (2017). Sensitivity of transatlantic dust transport to chemical
595 aging and related atmospheric processes. *Atmospheric Chemistry and Physics*, 17(6), 3799–
596 3821. <https://doi.org/10.5194/acp-17-3799-2017>

597 Albrecht, B. A. (1989). Aerosols, cloud microphysics, and fractional cloudiness. *Science*,
598 245(4923), 1227–1230. <https://doi.org/10.1126/science.245.4923.1227>

599 Andreae, M O, Elbert, W., Gabriel, R., Johnson, D. W., Osborne, S., & Wood, R. (2000).
600 Soluble ion chemistry of the atmospheric aerosol and SO₂ concentrations over the eastern
601 North Atlantic during ACE-2. *Tellus B: Chemical and Physical Meteorology*.
602 <https://doi.org/10.3402/tellusb.v52i4.17087>

603 Andreae, Meinrat O. (1983). Soot Carbon and Excess Fine Potassium: Long-Range Transport of
604 Combustion-Derived Aerosols. *Science*, 220(4602), 1148–1151.
605 <https://doi.org/10.1126/science.220.4602.1148>

606 Andreae, Meinrat O, Charlson, R. J., Bruynseels, F., Storms, H., Grieken, R. Van, & Maenhaut,
607 W. (1986). Internal Mixture of Sea Salt, Silicates, and Excess Sulfate in Marine Aerosols.
608 *Science*, 232(4758), 1620–1623. <https://doi.org/10.1126/science.232.4758.1620>

609 Archibald, A. T., Witham, C. S., Ashfold, M. J., Manning, A. J., O’Doherty, S., Grealley, B. R.,
610 Young, D., & Shallcross, D. E. (2015). Long-term high frequency measurements of ethane,
611 benzene and methyl chloride at Ragged Point, Barbados: Identification of long-range
612 transport events. *Elementa: Science of the Anthropocene*, 3.
613 <https://doi.org/10.12952/journal.elementa.000068>

614 Archuleta, C. M., DeMott, P. J., & Kreidenweis, S. M. (2005). Ice nucleation by surrogates for
615 atmospheric mineral dust and mineral dust/sulfate particles at cirrus temperatures.
616 *Atmospheric Chemistry and Physics*, 5(10), 2617–2634. <https://doi.org/10.5194/acp-5-2617-2005>

618 Ault, A. P., Peters, T. M., Sawvel, E. J., Casuccio, G. S., Willis, R. D., Norris, G. A., & Grassian,
619 V. H. (2012). Single-Particle SEM-EDX Analysis of Iron-Containing Coarse Particulate
620 Matter in an Urban Environment: Sources and Distribution of Iron within Cleveland, Ohio.
621 *Environmental Science & Technology*, 46(8), 4331–4339.
622 <https://doi.org/10.1021/es204006k>

623 Ault, A. P., Moffet, R. C., Baltrusaitis, J., Collins, D. B., Ruppel, M. J., Cuadra-Rodriguez, L.
624 A., Zhao, D., Guasco, T. L., Ebben, C. J., Geiger, F. M., Bertram, T. H., Prather, K. A., &
625 Grassian, V. H. (2013). Size-Dependent Changes in Sea Spray Aerosol Composition and
626 Properties with Different Seawater Conditions. *Environmental Science & Technology*,
627 47(11), 5603–5612. <https://doi.org/10.1021/es400416g>

628 Ault, A. P., Guasco, T. L., Baltrusaitis, J., Ryder, O. S., Trueblood, J. V, Collins, D. B., Ruppel,
629 M. J., Cuadra-Rodriguez, L. A., Prather, K. A., & Grassian, V. H. (2014). Heterogeneous
630 Reactivity of Nitric Acid with Nascent Sea Spray Aerosol: Large Differences Observed
631 between and within Individual Particles. *The Journal of Physical Chemistry Letters*, 5(15),
632 2493–2500. <https://doi.org/10.1021/jz5008802>

633 Baker, A. R., & Jickells, T. D. (2006). Mineral particle size as a control on aerosol iron



- 634 solubility. *Geophysical Research Letters*, 33(17), 1–4.
635 <https://doi.org/10.1029/2006GL026557>
- 636 Balkanski, Y., Schulz, M., Claquin, T., & Guibert, S. (2007). Reevaluation of Mineral aerosol
637 radiative forcings suggests a better agreement with satellite and AERONET data.
638 *Atmospheric Chemistry and Physics*, 7(1), 81–95. <https://doi.org/10.5194/acp-7-81-2007>
- 639 Barkley, A. E., Prospero, J. M., Mahowald, N., Hamilton, D. S., Popendorf, K. J., Oehlert, A.
640 M., Pourmand, A., Gatineau, A., Panechou-Pulcherie, K., Blackwelder, P., & Gaston, C. J.
641 (2019). African biomass burning is a substantial source of phosphorus deposition to the
642 Amazon, Tropical Atlantic Ocean, and Southern Ocean. *Proceedings of the National*
643 *Academy of Sciences*, 116(33), 16216 LP – 16221. <https://doi.org/10.1073/pnas.1906091116>
- 644 Bauer, S. E., Mishchenko, M. I., Laciš, A. A., Zhang, S., Perlwitz, J., & Metzger, S. M. (2007).
645 Do sulfate and nitrate coatings on mineral dust have important effects on radiative
646 properties and climate modeling? *Journal of Geophysical Research: Atmospheres*, 112(D6).
647 <https://doi.org/https://doi.org/10.1029/2005JD006977>
- 648 Behnke, W., George, C., Scheer, V., & Zetzsch, C. (1997). Production and decay of ClNO₂ from
649 the reaction of gaseous N₂O₅ with NaCl solution: Bulk and aerosol experiments. *Journal of*
650 *Geophysical Research Atmospheres*, 102(3), 3795–3804. <https://doi.org/10.1029/96jd03057>
- 651 Bondy, A L, Bonanno, D., Moffet, R. C., Wang, B., Laskin, A., & Ault, A. P. (2018). The
652 diverse chemical mixing state of aerosol particles in the southeastern United States.
653 *Atmospheric Chemistry and Physics*, 18(16), 12595–12612. [https://doi.org/10.5194/acp-18-](https://doi.org/10.5194/acp-18-12595-2018)
654 [12595-2018](https://doi.org/10.5194/acp-18-12595-2018)
- 655 Bondy, Amy L, Wang, B., Laskin, A., Craig, R. L., Nhiziyo, M. V, Bertman, S. B., Pratt, K. A.,
656 Shepson, P. B., & Ault, A. P. (2017). Inland Sea Spray Aerosol Transport and Incomplete
657 Chloride Depletion: Varying Degrees of Reactive Processing Observed during SOAS.
658 *Environmental Science & Technology*, 51(17), 9533–9542.
659 <https://doi.org/10.1021/acs.est.7b02085>
- 660 Carlson, T. N., & Prospero, J. M. (1972). The Large-Scale Movement of Saharan Air Outbreaks
661 over the Northern Equatorial Atlantic. *Journal of Applied Meteorology and Climatology*,
662 11(2), 283–297. [https://doi.org/10.1175/1520-0450\(1972\)011<0283:TLSMOS>2.0.CO;2](https://doi.org/10.1175/1520-0450(1972)011<0283:TLSMOS>2.0.CO;2)
- 663 Chen, Y., & Siefert, R. L. (2004). Seasonal and spatial distributions and dry deposition fluxes of
664 atmospheric total and labile iron over the tropical and subtropical North Atlantic Ocean.
665 *Journal of Geophysical Research: Atmospheres*, 109(D9).
666 <https://doi.org/https://doi.org/10.1029/2003JD003958>
- 667 Chiapello, I., Bergametti, G., Gomes, L., Chatenet, B., Dulac, F., Pimenta, J., & Soares, E. S.
668 (1995). An additional low layer transport of Sahelian and Saharan dust over the north-
669 eastern Tropical Atlantic. *Geophysical Research Letters*, 22(23), 3191–3194.
670 <https://doi.org/https://doi.org/10.1029/95GL03313>
- 671 Choël, M., Deboudt, K., Flament, P., Aimo, L., & Mériaux, X. (2007). Single-particle analysis
672 of atmospheric aerosols at Cape Gris-Nez, English Channel: Influence of steel works on
673 iron apportionment. *Atmospheric Environment*, 41(13), 2820–2830.
674 <https://doi.org/https://doi.org/10.1016/j.atmosenv.2006.11.038>
- 675 Cziczo, D. J., Murphy, D. M., Hudson, P. K., & Thomson, D. S. (2004). Single particle
676 measurements of the chemical composition of cirrus ice residue during CRYSTAL-FACE.
677 *Journal of Geophysical Research: Atmospheres*, 109(D4).
678 <https://doi.org/https://doi.org/10.1029/2003JD004032>
- 679 DeMott, P. J., Sassen, K., Poellot, M. R., Baumgardner, D., Rogers, D. C., Brooks, S. D., Prenni,



- 680 A. J., & Kreidenweis, S. M. (2003). African dust aerosols as atmospheric ice nuclei.
681 *Geophysical Research Letters*, 30(14).
682 <https://doi.org/https://doi.org/10.1029/2003GL017410>
- 683 Denjean, C., Caquineau, S., Desboeufs, K., Laurent, B., Maille, M., Quiñones Rosado, M.,
684 Vallejo, P., Mayol-Bracero, O. L., & Formenti, P. (2015). Long-range transport across the
685 Atlantic in summertime does not enhance the hygroscopicity of African mineral dust.
686 *Geophysical Research Letters*, 42(18), 7835–7843.
687 <https://doi.org/https://doi.org/10.1002/2015GL065693>
- 688 Desboeufs, K., Formenti, P., Torres-Sánchez, R., Schepanski, K., Chaboureau, J.-P., Andersen,
689 H., Cermak, J., Feuerstein, S., Laurent, B., Klopfer, D., Namwoonde, A., Cazaunau, M.,
690 Chevaillier, S., Feron, A., Mirande-Bret, C., Triquet, S., & Piketh, S. J. (2024). Fractional
691 solubility of iron in mineral dust aerosols over coastal Namibia: a link to marine biogenic
692 emissions? *Atmospheric Chemistry and Physics*, 24(2), 1525–1541.
693 <https://doi.org/10.5194/acp-24-1525-2024>
- 694 Elliott, H. E., Pependorf, K. J., Blades, E., Royer, H. M., Pollier, C. G. L., Oehlert, A. M.,
695 Kukkadapu, R., Ault, A., & Gaston, C. J. (2024). Godzilla mineral dust and La Soufrière
696 volcanic ash fallout immediately stimulate marine microbial phosphate uptake, 10.
697 <https://doi.org/https://doi.org/10.3389/fmars.2023.1308689>
- 698 Fitzgerald, E., Ault, A. P., Zauscher, M. D., Mayol-Bracero, O. L., & Prather, K. A. (2015).
699 Comparison of the mixing state of long-range transported Asian and African mineral dust.
700 *Atmospheric Environment*, 115, 19–25.
701 <https://doi.org/https://doi.org/10.1016/j.atmosenv.2015.04.031>
- 702 Gaston, C. J. (2020). Re-examining Dust Chemical Aging and Its Impacts on Earth's Climate.
703 *Accounts of Chemical Research*, 53(5), 1005–1013.
704 <https://doi.org/10.1021/acs.accounts.0c00102>
- 705 Gaston, C. J., Pratt, K. A., Qin, X., & Prather, K. A. (2010). Real-time detection and mixing state
706 of methanesulfonate in single particles at an inland urban location during a phytoplankton
707 bloom. *Environmental Science and Technology*, 44(5), 1566–1572.
708 <https://doi.org/10.1021/es902069d>
- 709 Gaston, C. J., Furutani, H., Guazzotti, S. A., Coffee, K. R., Bates, T. S., Quinn, P. K., Aluwihare,
710 L. I., Mitchell, B. G., & Prather, K. A. (2011). Unique ocean-derived particles serve as a
711 proxy for changes in ocean chemistry. *Journal of Geophysical Research Atmospheres*,
712 116(18), 1–13. <https://doi.org/10.1029/2010JD015289>
- 713 Gaston, C. J., Quinn, P. K., Bates, T. S., Gilman, J. B., Bon, D. M., Kuster, W. C., & Prather, K.
714 A. (2013). The impact of shipping, agricultural, and urban emissions on single particle
715 chemistry observed aboard the R/V Atlantis during CalNex. *Journal of Geophysical
716 Research Atmospheres*, 118(10), 5003–5017. <https://doi.org/10.1002/jgrd.50427>
- 717 Gibson, E. R., Gierlus, K. M., Hudson, P. K., & Grassian, V. H. (2007). Generation of Internally
718 Mixed Insoluble and Soluble Aerosol Particles to Investigate the Impact of Atmospheric
719 Aging and Heterogeneous Processing on the CCN Activity of Mineral Dust Aerosol.
720 *Aerosol Science and Technology*, 41(10), 914–924.
721 <https://doi.org/10.1080/02786820701557222>
- 722 Gierlus, K. M., Laskina, O., Abernathy, T. L., & Grassian, V. H. (2012). Laboratory study of the
723 effect of oxalic acid on the cloud condensation nuclei activity of mineral dust aerosol.
724 *Atmospheric Environment*, 46, 125–130.
725 <https://doi.org/https://doi.org/10.1016/j.atmosenv.2011.10.027>



- 726 Gutleben, M., Groß, S., Heske, C., & Wirth, M. (2022). Wintertime Saharan dust transport
727 towards the Caribbean: an airborne lidar case study during EUREC⁴A. *Atmospheric*
728 *Chemistry and Physics*, 22(11), 7319–7330. <https://doi.org/10.5194/acp-22-7319-2022>
- 729 Han, X., Zhang, M., Han, Z., Xin, J., & Liu, X. (2011). Simulation of aerosol direct radiative
730 forcing with RAMS-CMAQ in East Asia. *Atmospheric Environment*, 45(36), 6576–6592.
731 <https://doi.org/https://doi.org/10.1016/j.atmosenv.2011.08.006>
- 732 Hand, V. L., Capes, G., Vaughan, D. J., Formenti, P., Haywood, J. M., & Coe, H. (2010).
733 Evidence of internal mixing of African dust and biomass burning particles by individual
734 particle analysis using electron beam techniques. *Journal of Geophysical Research:*
735 *Atmospheres*, 115(D13). <https://doi.org/https://doi.org/10.1029/2009JD012938>
- 736 Haywood, J., Francis, P., Osborne, S., Glew, M., Loeb, N., Highwood, E., Tanré, D., Myhre, G.,
737 Formenti, P., & Hirst, E. (2003). Radiative properties and direct radiative effect of Saharan
738 dust measured by the C-130 aircraft during SHADE: 1. Solar spectrum. *Journal of*
739 *Geophysical Research: Atmospheres*, 108(D18).
740 <https://doi.org/https://doi.org/10.1029/2002JD002687>
- 741 Hickman, J. E., Andela, N., Tsigaridis, K., Galy-Lacaux, C., Osohou, M., & Bauer, S. E.
742 (2021). Reductions in NO₂ burden over north equatorial Africa from decline in biomass
743 burning in spite of growing fossil fuel use, 2005 to 2017. *Proceedings of the National*
744 *Academy of Sciences*, 118(7), e2002579118. <https://doi.org/10.1073/pnas.2002579118>
- 745 Hopkins, R. J., Desyaterik, Y., Tivanski, A. V., Zaveri, R. A., Berkowitz, C. M., Tyliszczak, T.,
746 Gilles, M. K., & Laskin, A. (2008). Chemical speciation of sulfur in marine cloud droplets
747 and particles: Analysis of individual particles from the marine boundary layer over the
748 California current. *Journal of Geophysical Research: Atmospheres*, 113(D4).
749 <https://doi.org/https://doi.org/10.1029/2007JD008954>
- 750 Jickells, T. D., An, Z. S., Andersen, K. K., Baker, A. R., Bergametti, G., Brooks, N., Cao, J. J.,
751 Boyd, P. W., Duce, R. A., Hunter, K. A., Kawahata, H., Kubilay, N., laRoche, J., Liss, P. S.,
752 Mahowald, N., Prospero, J. M., Ridgwell, A. J., Tegen, I., & Torres, R. (2005). Global Iron
753 Connections Between Desert Dust, Ocean Biogeochemistry, and Climate. *Science*,
754 308(5718), 67–71. <https://doi.org/10.1126/science.1105959>
- 755 Kandler, K., Lieke, K., Benker, N., Emmel, C., Küpper, M., Müller-Ebert, D., Ebert, M.,
756 Scheuvs, D., Schladitz, A., Schütz, L., & Weinbruch, S. (2011). Electron microscopy of
757 particles collected at Praia, Cape Verde, during the Saharan Mineral Dust Experiment:
758 particle chemistry, shape, mixing state and complex refractive index. *Tellus B: Chemical*
759 *and Physical Meteorology*, 63(4), 475–496. <https://doi.org/10.1111/j.1600-0889.2011.00550.x>
- 760
761 Kandler, K., Schneiders, K., Ebert, M., Hartmann, M., Weinbruch, S., Prass, M., & Pöhlker, C.
762 (2018). Composition and mixing state of atmospheric aerosols determined by electron
763 microscopy: method development and application to aged Saharan dust deposition in the
764 Caribbean boundary layer. *Atmos. Chem. Phys.*, 18(18), 13429–13455.
765 <https://doi.org/10.5194/acp-18-13429-2018>
- 766 Kelly, J. T., Chuang, C. C., & Wexler, A. S. (2007). Influence of dust composition on cloud
767 droplet formation. *Atmospheric Environment*, 41(14), 2904–2916.
768 <https://doi.org/10.1016/j.atmosenv.2006.12.008>
- 769 Koehler, K. A., Kreidenweis, S. M., DeMott, P. J., Petters, M. D., Prenni, A. J., & Carrico, C. M.
770 (2009). Hygroscopicity and cloud droplet activation of mineral dust aerosol. *Geophysical*
771 *Research Letters*, 36(8). <https://doi.org/https://doi.org/10.1029/2009GL037348>



- 772 Krueger, B. J., Grassian, V. H., Laskin, A., & Cowin, J. P. (2003). The transformation of solid
773 atmospheric particles into liquid droplets through heterogeneous chemistry: Laboratory
774 insights into the processing of calcium containing mineral dust aerosol in the troposphere.
775 *Geophysical Research Letters*, 30(3). [https://doi.org/https://doi.org/10.1029/2002GL016563](https://doi.org/10.1029/2002GL016563)
- 776 Krueger, B. J., Grassian, V. H., Cowin, J. P., & Laskin, A. (2004). Heterogeneous chemistry of
777 individual mineral dust particles from different dust source regions: The importance of
778 particle mineralogy. *Atmospheric Environment*, 38(36), 6253–6261.
779 <https://doi.org/10.1016/j.atmosenv.2004.07.010>
- 780 Lance, S., Raatikainen, T., Onasch, T. B., Worsnop, D. R., Yu, X.-Y., Alexander, M. L.,
781 Stolzenburg, M. R., McMurry, P. H., Smith, J. N., & Nenes, A. (2013). Aerosol mixing
782 state, hygroscopic growth and cloud activation efficiency during MIRAGE 2006.
783 *Atmospheric Chemistry and Physics*, 13(9), 5049–5062. <https://doi.org/10.5194/acp-13-5049-2013>
- 784
- 785 Laskin, A., Wietsma, T. W., Krueger, B. J., & Grassian, V. H. (2005). Heterogeneous chemistry
786 of individual mineral dust particles with nitric acid: A combined CCSEM/EDX, ESEM, and
787 ICP-MS study. *Journal of Geophysical Research: Atmospheres*, 110(D10).
788 [https://doi.org/https://doi.org/10.1029/2004JD005206](https://doi.org/10.1029/2004JD005206)
- 789 Laskin, Alexander, Moffet, R. C., Gilles, M. K., Fast, J. D., Zaveri, R. A., Wang, B., Nigge, P.,
790 & Shutthanandan, J. (2012). Tropospheric chemistry of internally mixed sea salt and
791 organic particles: Surprising reactivity of NaCl with weak organic acids. *Journal of*
792 *Geophysical Research: Atmospheres*, 117(D15).
793 [https://doi.org/https://doi.org/10.1029/2012JD017743](https://doi.org/10.1029/2012JD017743)
- 794 Levin, Z., Teller, A., Ganor, E., & Yin, Y. (2005). On the interactions of mineral dust, sea-salt
795 particles, and clouds: A measurement and modeling study from the Mediterranean Israeli
796 Dust Experiment campaign. *Journal of Geophysical Research: Atmospheres*, 110(D20).
797 [https://doi.org/https://doi.org/10.1029/2005JD005810](https://doi.org/10.1029/2005JD005810)
- 798 Levin, Zev, Ganor, E., & Gladstein, V. (1996). The Effects of Desert Particles Coated with
799 Sulfate on Rain Formation in the Eastern Mediterranean. *Journal of Applied Meteorology*
800 *and Climatology*, 35(9), 1511–1523. [https://doi.org/https://doi.org/10.1175/1520-0450\(1996\)035<1511:TEODPC>2.0.CO;2](https://doi.org/10.1175/1520-0450(1996)035<1511:TEODPC>2.0.CO;2)
- 801
- 802 Li-Jones, X., & Prospero, J. M. (1998). Variations in the size distribution of non-sea-salt sulfate
803 aerosol in the marine boundary layer at Barbados: Impact of African dust. *Journal of*
804 *Geophysical Research: Atmospheres*, 103(D13), 16073–16084.
805 [https://doi.org/https://doi.org/10.1029/98JD00883](https://doi.org/10.1029/98JD00883)
- 806 Li, J., Pósfai, M., Hobbs, P. V., & Buseck, P. R. (2003). Individual aerosol particles from
807 biomass burning in southern Africa: 2, Compositions and aging of inorganic particles.
808 *Journal of Geophysical Research: Atmospheres*, 108(D13).
809 [https://doi.org/https://doi.org/10.1029/2002JD002310](https://doi.org/10.1029/2002JD002310)
- 810 Li, W., Shao, L., Shi, Z., Chen, J., Yang, L., Yuan, Q., Yan, C., Zhang, X., Wang, Y., Sun, J.,
811 Zhang, Y., Shen, X., Wang, Z., & Wang, W. (2014). Mixing state and hygroscopicity of
812 dust and haze particles before leaving Asian continent. *Journal of Geophysical Research:*
813 *Atmospheres*, 119(2), 1044–1059. [https://doi.org/https://doi.org/10.1002/2013JD021003](https://doi.org/10.1002/2013JD021003)
- 814 Li, Y., Zhou, Y., Guo, W., Zhang, X., Huang, Y., He, E., Li, R., Yan, B., Wang, H., Mei, F., Liu,
815 M., & Zhu, Z. (2023). Molecular Imaging Reveals Two Distinct Mixing States of PM_{2.5}
816 Particles Sampled in a Typical Beijing Winter Pollution Case. *Environmental Science &*
817 *Technology*, 57(15), 6273–6283. <https://doi.org/10.1021/acs.est.2c08694>



- 818 Ma, C.-J., Tohno, S., Kasahara, M., & Hayakawa, S. (2004). Properties of the size-resolved and
819 individual cloud droplets collected in western Japan during the Asian dust storm event.
820 *Atmospheric Environment*, 38(27), 4519–4529.
821 <https://doi.org/https://doi.org/10.1016/j.atmosenv.2004.05.032>
- 822 Mahowald, N. (2011). Aerosol Indirect Effect on Biogeochemical Cycles and Climate. *Science*,
823 334(6057), 794–796. <https://doi.org/10.1126/science.1207374>
- 824 Metzger, S., Mihalopoulos, N., & Lelieveld, J. (2006). Importance of mineral cations and
825 organics in gas-aerosol partitioning of reactive nitrogen compounds: case study based on
826 MINOS results. *Atmospheric Chemistry and Physics*, 6(9), 2549–2567.
827 <https://doi.org/10.5194/acp-6-2549-2006>
- 828 Myhre, G., & Stordal, F. (2001). Global sensitivity experiment of the radiative forcing due to
829 mineral aerosols. *Journal of Geophysical Research*, 106, 18193–18204.
830 <https://doi.org/10.1029/2000JD900536>
- 831 Nenes, A., Krom, M. D., Mihalopoulos, N., Van Cappellen, P., Shi, Z., Bougiatioti, A., Zarmas,
832 P., & Herut, B. (2011). Atmospheric acidification of mineral aerosols: a source of
833 bioavailable phosphorus for the oceans. *Atmospheric Chemistry and Physics*, 11(13), 6265–
834 6272. <https://doi.org/10.5194/acp-11-6265-2011>
- 835 Pringle, K. J., Tost, H., Pozzer, A., Pöschl, U., & Lelieveld, J. (2010). Global distribution of the
836 effective aerosol hygroscopicity parameter for CCN activation. *Atmospheric Chemistry and
837 Physics*, 10(12), 5241–5255. <https://doi.org/10.5194/acp-10-5241-2010>
- 838 Prospero, J. M. (1968). atmospheric dust studies on Barbados. *Bulletin of the American
839 Meteorological Society*, 49(6), 645–652. <https://doi.org/10.1175/1520-0477-49.6.645>
- 840 Prospero, J. M., & Mayol-Bracero, O. L. (2013). Understanding the transport and impact of
841 African dust on the Caribbean Basin. *Bulletin of the American Meteorological Society*,
842 94(9), 1329–1337. <https://doi.org/10.1175/BAMS-D-12-00142.1>
- 843 Prospero, J. M. (1999). Long-range transport of mineral dust in the global atmosphere: Impact of
844 African dust on the environment of the southeastern United States. *Proceedings of the
845 National Academy of Sciences*, 96(7), 3396 LP – 3403.
846 <https://doi.org/10.1073/pnas.96.7.3396>
- 847 Prospero, J. M., Blades, E., Mathison, G., & Naidu, R. (2005). Interhemispheric transport of
848 viable fungi and bacteria from Africa to the Caribbean with soil dust. *Aerobiologia*, 21(1),
849 1–19. <https://doi.org/10.1007/s10453-004-5872-7>
- 850 Prospero, J. M., Delany, A. C., Delany, A. C., & Carlson, T. N. (2021). The Discovery of African
851 Dust Transport to the Western Hemisphere and the Saharan Air Layer: A History. *Bulletin
852 of the American Meteorological Society*, 102(6), E1239–E1260.
853 <https://doi.org/10.1175/BAMS-D-19-0309.1>
- 854 Quinn, P. K., Thompson, E. J., Coffman, D. J., Baidar, S., Bariteau, L., Bates, T. S., Bigorre, S.,
855 Brewer, A., de Boer, G., de Szoeko, S. P., Drushka, K., Foltz, G. R., Intrieri, J., Iyer, S.,
856 Fairall, C. W., Gaston, C. J., Jansen, F., Johnson, J. E., Krüger, O. O., Marchbanks, R. D.,
857 Moran, K. P., Noone, D., Pezoa, S., Pincus, R., Plueddemann, A. J., Pöhlker, M. L., Pöschl,
858 U., Quinones Melendez, E., Royer, H. M., Szczodrak, M., Thomson, J., Upchurch, L. M.,
859 Zhang, C., Zhang, D., & Zuidema, P. (2021). Measurements from the RV Ronald H. Brown
860 and related platforms as part of the Atlantic Tradewind Ocean-Atmosphere Mesoscale
861 Interaction Campaign (ATOMIC). *Earth Syst. Sci. Data*, 13(4), 1759–1790.
862 <https://doi.org/10.5194/essd-13-1759-2021>
- 863 Rickly, P. S., Guo, H., Campuzano-Jost, P., Jimenez, J. L., Wolfe, G. M., Bennett, R., Bourgeois,



- 864 I., Crounse, J. D., Dibb, J. E., DiGangi, J. P., Diskin, G. S., Dollner, M., Gargulinski, E. M.,
865 Hall, S. R., Halliday, H. S., Hanisco, T. F., Hannun, R. A., Liao, J., Moore, R., Nault, B. A.,
866 Nowak, J. B., Peischl, J., Robinson, C. E., Ryerson, T., Sanchez, K. J., Schöberl, M., Soja,
867 A. J., St. Clair, J. M., Thornhill, K. L., Ullmann, K., Wennberg, P. O., Weinzierl, B.,
868 Wiggins, E. B., Winstead, E. L., & Rollins, A. W. (2022). Emission factors and evolution of
869 SO₂ measured from biomass burning in wildfires and agricultural fires. *Atmospheric*
870 *Chemistry and Physics*, 22(23), 15603–15620. <https://doi.org/10.5194/acp-22-15603-2022>
871 Rosenfeld, D., Rudich, Y., & Lahav, R. (2001). Desert dust suppressing precipitation: A possible
872 desertification feedback loop. *Proceedings of the National Academy of Sciences*, 98(11),
873 5975 LP – 5980. <https://doi.org/10.1073/pnas.101122798>
874 Royer, H. M., Pöhlker, M. L., Krüger, O., Blades, E., Sealy, P., Lata, N. N., Cheng, Z., China, S.,
875 Ault, A. P., Quinn, P. K., Zuidema, P., Pöhlker, C., Pöschl, U., Andreae, M., & Gaston, C.
876 J. (2023). African smoke particles act as cloud condensation nuclei in the wintertime
877 tropical North Atlantic boundary layer over Barbados. *Atmospheric Chemistry and Physics*,
878 23(2), 981–998. <https://doi.org/10.5194/acp-23-981-2023>
879 Ryder, C. L., Marengo, F., Brooke, J. K., Estelles, V., Cotton, R., Formenti, P., McQuaid, J. B.,
880 Price, H. C., Liu, D., Ausset, P., Rosenberg, P. D., Taylor, J. W., Choulaton, T., Bower, K.,
881 Coe, H., Gallagher, M., Crosier, J., Lloyd, G., Highwood, E. J., & Murray, B. J. (2018).
882 Coarse-mode mineral dust size distributions, composition and optical properties from AER-
883 D aircraft measurements over the tropical eastern Atlantic. *Atmospheric Chemistry and*
884 *Physics*, 18(23), 17225–17257. <https://doi.org/10.5194/acp-18-17225-2018>
885 Savoie, D L., & Prospero, J. M. (1982). Particle size distribution of nitrate and sulfate in the
886 marine atmosphere. *Geophysical Research Letters*, 9(10), 1207–1210.
887 <https://doi.org/https://doi.org/10.1029/GL009i010p01207>
888 Savoie, Dennis L, Arimoto, R., Keene, W. C., Prospero, J. M., Duce, R. A., & Galloway, J. N.
889 (2002). Marine biogenic and anthropogenic contributions to non-sea-salt sulfate in the
890 marine boundary layer over the North Atlantic Ocean. *Journal of Geophysical Research:*
891 *Atmospheres*, 107(D18), AAC 3-1-AAC 3-21.
892 <https://doi.org/https://doi.org/10.1029/2001JD000970>
893 Shen, H., Peters, T. M., Casuccio, G. S., Lersch, T. L., West, R. R., Kumar, A., Kumar, N., &
894 Ault, A. P. (2016). Elevated Concentrations of Lead in Particulate Matter on the
895 Neighborhood-Scale in Delhi, India As Determined by Single Particle Analysis.
896 *Environmental Science & Technology*, 50(10), 4961–4970.
897 <https://doi.org/10.1021/acs.est.5b06202>
898 Shi, Z., Zhang, D., Hayashi, M., Ogata, H., Ji, H., & Fujie, W. (2008). Influences of sulfate and
899 nitrate on the hygroscopic behaviour of coarse dust particles. *Atmospheric Environment*,
900 42(4), 822–827. <https://doi.org/https://doi.org/10.1016/j.atmosenv.2007.10.037>
901 Sobanska, S., Coeur, C., Maenhaut, W., & Adams, F. (2003). SEM-EDX Characterisation of
902 Tropospheric Aerosols in the Negev Desert (Israel). *Journal of Atmospheric Chemistry*,
903 44(3), 299–322. <https://doi.org/10.1023/A:1022969302107>
904 Sokolik, I. N., Winker, D. M., Bergametti, G., Gillette, D. A., Carmichael, G., Kaufman, Y. J.,
905 Gomes, L., Schuetz, L., & Penner, J. E. (2001). Introduction to special section: Outstanding
906 problems in quantifying the radiative impacts of mineral dust. *Journal of Geophysical*
907 *Research: Atmospheres*, 106(D16), 18015–18027.
908 <https://doi.org/https://doi.org/10.1029/2000JD900498>
909 Spokes, L. J., & Jickells, T. D. (1995). Factors controlling the solubility of aerosol trace metals



910 in the atmosphere and on mixing into seawater. *Aquatic Geochemistry*, 1(4), 355–374.
911 <https://doi.org/10.1007/BF00702739>
912 Stevens, B., Bony, S., Farrell, D., Ament, F., Blyth, A., Fairall, C., Karstensen, J., Quinn, P. K.,
913 Speich, S., Acquistapace, C., Aemisegger, F., Albright, A. L., Bellenger, H., Bodenschatz,
914 E., Caesar, K.-A., Chewitt-Lucas, R., de Boer, G., Delanoë, J., Denby, L., Ewald, F.,
915 Fildier, B., Forde, M., George, G., Gross, S., Hagen, M., Hausold, A., Heywood, K. J.,
916 Hirsch, L., Jacob, M., Jansen, F., Kinne, S., Klocke, D., Kölling, T., Konow, H., Lathon,
917 M., Mohr, W., Naumann, A. K., Nuijens, L., Olivier, L., Pincus, R., Pöhlker, M., Reverdin,
918 G., Roberts, G., Schnitt, S., Schulz, H., Siebesma, A. P., Stephan, C. C., Sullivan, P.,
919 Touzé-Peiffer, L., Vial, J., Vogel, R., Zuidema, P., Alexander, N., Alves, L., Arixi, S.,
920 Asmath, H., Bagheri, G., Baier, K., Bailey, A., Baranowski, D., Baron, A., Barrau, S.,
921 Barrett, P. A., Batier, F., Behrendt, A., Bendinger, A., Beucher, F., Bigorre, S., Blades, E.,
922 Blossey, P., Bock, O., Böing, S., Bosser, P., Bourras, D., Bouruet-Aubertot, P., Bower, K.,
923 Branellec, P., Branger, H., Brennek, M., Brewer, A., Brilouet, P.-E., Brüggmann, B.,
924 Buehler, S. A., Burke, E., Burton, R., Calmer, R., Canonici, J.-C., Carton, X., Cato Jr., G.,
925 Charles, J. A., Chazette, P., Chen, Y., Chilinski, M. T., Choularton, T., Chuang, P., Clarke,
926 S., Coe, H., Cornet, C., Coutris, P., Couvreur, F., Crewell, S., Cronin, T., Cui, Z., Cuyppers,
927 Y., Daley, A., Damerell, G. M., Dauhut, T., Deneke, H., Desbios, J.-P., Dörner, S., Donner,
928 S., Douet, V., Drushka, K., Dütsch, M., Ehrlich, A., Emanuel, K., Emmanouilidis, A.,
929 Etienne, J.-C., Etienne-Leblanc, S., Faure, G., Feingold, G., Ferrero, L., Fix, A., Flamant,
930 C., Flatau, P. J., Foltz, G. R., Forster, L., Furtuna, I., Gadian, A., Galewsky, J., Gallagher,
931 M., Gallimore, P., Gaston, C., Gentemann, C., Geyskens, N., Giez, A., Gollop, J., Gouirand,
932 I., Gourbeyre, C., de Graaf, D., de Groot, G. E., Grosz, R., Güttler, J., Gutleben, M., Hall,
933 K., Harris, G., Helfer, K. C., Henze, D., Herbert, C., Holanda, B., Ibanez-Landeta, A.,
934 Intrieri, J., Iyer, S., Julien, F., Kalesse, H., Kazil, J., Kellman, A., Kidane, A. T., Kirchner,
935 U., Klingebiel, M., Körner, M., Kremper, L. A., Kretzschmar, J., Krüger, O., Kumala, W.,
936 Kurz, A., L'Hégaret, P., Labaste, M., Lachlan-Cope, T., Laing, A., Landschützer, P., Lang,
937 T., Lange, D., Lange, I., Laplace, C., Lavik, G., Laxenaire, R., Le Bihan, C., Leandro, M.,
938 Lefevre, N., Lena, M., Lenschow, D., Li, Q., Lloyd, G., Los, S., Losi, N., Lovell, O.,
939 Luneau, C., Makuch, P., Malinowski, S., Manta, G., Marinou, E., Marsden, N., Masson, S.,
940 Maury, N., Mayer, B., Mayers-Als, M., Mazel, C., McGeary, W., McWilliams, J. C., Mech,
941 M., Mehlmann, M., Meroni, A. N., Mieslinger, T., Minikin, A., Minnett, P., Möller, G.,
942 Morfa Avalos, Y., Muller, C., Musat, I., Napoli, A., Neuberger, A., Noisel, C., Noone, D.,
943 Nordsiek, F., Nowak, J. L., Oswald, L., Parker, D. J., Peck, C., Person, R., Philippi, M.,
944 Plueddemann, A., Pöhlker, C., Pörtge, V., Pöschl, U., Pologne, L., Posyniak, M., Prange,
945 M., Quiñones Meléndez, E., Radtke, J., Ramage, K., Reimann, J., Renault, L., Reus, K.,
946 Reyes, A., Ribbe, J., Ringel, M., Ritschel, M., Rocha, C. B., Rochetin, N., Röttenbacher, J.,
947 Rollo, C., Royer, H., Sadoulet, P., Saffin, L., Sandiford, S., Sandu, I., Schäfer, M.,
948 Schemann, V., Schirmacher, I., Schlenczek, O., Schmidt, J., Schröder, M.,
949 Schwarzenboeck, A., Sealy, A., Senff, C. J., Serikov, I., Shohan, S., Siddle, E., Smirnov, A.,
950 Späth, F., Spooner, B., Stolla, M. K., Szkółka, W., de Szoeko, S. P., Tarot, S., Tetoni, E.,
951 Thompson, E., Thomson, J., Tomassini, L., Totems, J., Ubele, A. A., Villiger, L., von Arx,
952 J., Wagner, T., Walther, A., Webber, B., Wendisch, M., Whitehall, S., Wiltshire, A., Wing,
953 A. A., Wirth, M., Wiskandt, J., Wolf, K., Worbes, L., Wright, E., Wulfmeyer, V., Young,
954 S., Zhang, C., Zhang, D., Ziemann, F., Zinner, T., & Zöger, M. (2021). EUREC4A. *Earth*
955 *Syst. Sci. Data*, 13(8), 4067–4119. <https://doi.org/10.5194/essd-13-4067-2021>



- 956 Stockdale, A., Krom, M. D., Mortimer, R. J. G., Benning, L. G., Carslaw, K. S., Herbert, R. J.,
957 Shi, Z., Myriokefalitakis, S., Kanakidou, M., & Nenes, A. (2016). Understanding the nature
958 of atmospheric acid processing of mineral dusts in supplying bioavailable phosphorus to the
959 oceans. *Proceedings of the National Academy of Sciences*, *113*(51), 14639–14644.
960 <https://doi.org/10.1073/pnas.1608136113>
- 961 Sullivan, R. C., Guazzotti, S. A., Sodeman, D. A., & Prather, K. A. (2007). Direct observations
962 of the atmospheric processing of Asian mineral dust. *Atmospheric Chemistry and Physics*,
963 *7*(5), 1213–1236. <https://doi.org/10.5194/acp-7-1213-2007>
- 964 Sullivan, R. C., Moore, M. J. K., Petters, M. D., Kreidenweis, S. M., Roberts, G. C., & Prather,
965 K. A. (2009). Effect of chemical mixing state on the hygroscopicity and cloud nucleation
966 properties of calcium mineral dust particles. *Atmospheric Chemistry and Physics*, *9*(10),
967 3303–3316. <https://doi.org/10.5194/acp-9-3303-2009>
- 968 Sullivan, R. C., & Prather, K. A. (2007). Investigations of the diurnal cycle and mixing state of
969 oxalic acid in individual particles in Asian aerosol outflow. *Environmental Science and*
970 *Technology*, *41*(23), 8062–8069. <https://doi.org/10.1021/es071134g>
- 971 Tegen, I. (2003). Modeling the mineral dust aerosol cycle in the climate system. *Quaternary*
972 *Science Reviews*, *22*(18), 1821–1834. [https://doi.org/https://doi.org/10.1016/S0277-](https://doi.org/https://doi.org/10.1016/S0277-3791(03)00163-X)
973 [3791\(03\)00163-X](https://doi.org/https://doi.org/10.1016/S0277-3791(03)00163-X)
- 974 Tsamalis, C., Chédin, A., Pelon, J., & Capelle, V. (2013). The seasonal vertical distribution of
975 the Saharan Air Layer and its modulation by the wind. *Atmos. Chem. Phys.*, *13*(22), 11235–
976 11257. <https://doi.org/10.5194/acp-13-11235-2013>
- 977 Ullerstam, M., Vogt, R., Langer, S., & Ljungström, E. (2002). The kinetics and mechanism of
978 SO₂ oxidation by O₃ on mineral dust. *Physical Chemistry Chemical Physics*, *4*(19), 4694–
979 4699. <https://doi.org/10.1039/B203529B>
- 980 Weinzierl, B., Ansmann, A., Prospero, J. M., Althausen, D., Benker, N., Chouza, F., Dollner, M.,
981 Farrell, D., Fomba, W. K., Freudenthaler, V., Gasteiger, J., Groß, S., Haarig, M., Heinold,
982 B., Kandler, K., Kristensen, T. B., Mayol-Bracero, O. L., Müller, T., Reitebuch, O., Sauer,
983 D., Schäfler, A., Schepanski, K., Spanu, A., Tegen, I., Toledano, C., & Walser, A. (2017).
984 The Saharan Aerosol Long-Range Transport and Aerosol–Cloud-Interaction Experiment:
985 Overview and Selected Highlights. *Bulletin of the American Meteorological Society*, *98*(7),
986 1427–1451. <https://doi.org/https://doi.org/10.1175/BAMS-D-15-00142.1>
- 987 Wu, Z., Birmili, W., Poulain, L., Wang, Z., Merkel, M., Fahlbusch, B., van Pinxteren, D.,
988 Herrmann, H., & Wiedensohler, A. (2013). Particle hygroscopicity during atmospheric new
989 particle formation events: implications for the chemical species contributing to particle
990 growth. *Atmospheric Chemistry and Physics*, *13*(13), 6637–6646.
991 <https://doi.org/10.5194/acp-13-6637-2013>
- 992 Wurzler, S., Reisin, T. G., & Levin, Z. (2000). Modification of mineral dust particles by cloud
993 processing and subsequent effects on drop size distributions. *Journal of Geophysical*
994 *Research: Atmospheres*, *105*(D4), 4501–4512.
995 <https://doi.org/https://doi.org/10.1029/1999JD900980>
- 996 Zuidema, P., Alvarez, C., Kramer, S. J., Custals, L., Izaguirre, M., Sealy, P., Prospero, J. M., &
997 Blades, E. (2019). Is Summer African Dust Arriving Earlier to Barbados? The Updated
998 Long-Term In Situ Dust Mass Concentration Time Series from Ragged Point, Barbados,
999 and Miami, Florida. *Bulletin of the American Meteorological Society*, *100*(10), 1981–1986.
1000 <https://doi.org/10.1175/BAMS-D-18-0083.1>
- 1001